

# Mid–infrared emission of galactic nuclei\*:

## TIMMI2 versus ISO observations and models

R. Siebenmorgen<sup>1</sup>, E. Krügel<sup>2</sup>, and H.W.W. Spoon<sup>3</sup>

<sup>1</sup> European Southern Observatory, Karl-Schwarzschildstr. 2, D-85748 Garching b. München, Germany

<sup>2</sup> Max-Planck-Institut für Radioastronomie, Auf dem Hügel 69, Postfach 2024, D-53010 Bonn, Germany

<sup>3</sup> Kapteyn Institute, P.O. Box 800, NL-9700 AV Groningen, The Netherlands

Received XXXX / Accepted XXXX

**Abstract.** We investigate the mid–infrared radiation of galaxies that are powered by a starburst or by an AGN. For this end, we compare the spectra obtained at different spatial scales in a sample of infrared bright galaxies. ISO observations which include emission of the nucleus as well as most of the host galaxy are compared with TIMMI2 spectra of the nuclear region. We find that ISO spectra are generally dominated by strong PAH bands. However, this is no longer true when inspecting the mid–infrared emission of the pure nucleus. Here PAH emission is detected in starbursts whereas it is significantly reduced or completely absent in AGNs. A physical explanation of these new observational results is presented by examining the temperature fluctuation of a PAH after interaction with a photon. It turns out that the hardness of the radiation field is a key parameter for quantifying the photo–destruction of small grains. Our theoretical study predicts PAH evaporation in soft X–ray environments. Radiative transfer calculations of clumpy starbursts and AGN corroborate the observational fact that PAH emission is connected to starburst activity whereas PAHs are destroyed near an AGN. The radiative transfer models predict for starbursts a much larger mid–infrared size than for AGN. This is confirmed by our TIMMI2 acquisition images: We find that the mid–infrared emission of Seyferts is dominated by a compact core while most of the starbursts are spatially resolved.

**Key words.** Infrared: galaxies – Galaxies: ISM – Galaxies: nuclei – Galaxies: dust

### 1. Introduction

Luminous infrared galaxies in the local universe with infrared luminosities exceeding  $10^{11} L_{\odot}$  were discovered in the IRAS all sky survey (Soifer et al. 1987). Responsible for their huge luminosity may be a combination of starburst and AGN activity. In both cases, the nuclear emission is fuelled by an enormous concentration of gas and dust in the central region (Sanders & Mirabel 1996).

Luminous infrared galaxies are also found to be a major component in the early universe ( $z \gtrsim 1$ ). Deep mid–infrared surveys with the infrared space observatory, ISO, could identify individual objects which account for most of the cosmic infrared background light. It is argued that the emission of most of the distant infrared galaxies comes mainly from starbursts (Elbaz et al. 2002). This hypoth-

esis may also be tested by inspecting the spectra of local galaxies. ISO spectra of local galaxies (Rigopoulou et al. 1999, Siebenmorgen et al. 1999, Clavel et al. 2000, Laureijs et al. 2000, Laurent et al. 2000) usually show a set of infrared emission bands which are attributed to the emission of polycyclic aromatic hydrocarbons (PAH).

The question as to which source, on average, is responsible for the luminosity of the cosmological background is still a matter of intense debate and, at the moment, different answers are given for different wavelength regions. The X–ray background could be partly resolved by ROSAT into individual components and Hasinger et al. (1998) showed that at X–rays AGNs make the greatest contribution. At infrared wavelengths, on the other hand, starbursts seem to dominate, as inferred from numerous ISO observations (Genzel & Cesarsky 2000).

We want to re-address the question whether infrared bright galaxies are predominantly powered by dust–enshrouded AGN or starbursts. As a new observational technique, we employ mid–infrared sub–arcsec imaging and mid–infrared spectroscopy at various spatial scales. (For previous ground based mid–infrared spectroscopy see

Send offprint requests to: rsiebenm@eso.org

\* Based on ESO: 68.B-0066(A) and observations with ISO, an ESA project with instruments funded by ESA Member States (especially the PI countries: France, Germany, the Netherlands and the United Kingdom) with the participation of ISAS and NASA.

for example: Smith et al. 1989, Roche et al. 1991 and Soifer et al. 2002). The mid-infrared wavelength region is of particular interest as the optical depth is usually sufficiently low to penetrate the dust enshrouded nucleus. Modern mid-infrared cameras have adequate spatial resolution to estimate the size of the emitting regions which is an important parameter to constrain the nature of the underlying source: At comparable distances of the sources a resolved mid-infrared emission points towards a starburst galaxy while an unresolved nucleus indicates an AGN or an extreme compact star cluster. As we will demonstrate in model calculations, infrared emission bands are a diagnostic tool to derive the activity type. The ratio of AGN versus starburst luminosity of local galaxies may be quantified by mid infrared spectra observed at different spatial resolutions.

The paper is structured as follows: In Sect. 2 we introduce the sample of infrared bright galaxies observed with ISO and TIMMI2. The observation are summarised in Sect. 3, the data analysis procedure is explained in Sect. 4. Observational results of individual galaxies are given in Sect. 5. Sect. 6 and 7 presents radiative transfer calculations, which also illustrate the effect of the optical depth on the SED, and a discussion of the heating and evaporation of PAH in starburst and AGN environments.

## 2. The sample

The ISO archive contains more than 250 galaxies that have been spectroscopically observed in the mid-infrared. We have selected 22 of these galaxies for observation with TIMMI2 to compare the large aperture ISO spectra to the narrow slit TIMMI2 spectra. The selected galaxies all have  $10\mu\text{m}$  ISO flux densities above  $\sim 100\text{mJy}$  and are visible from La Silla ( $-29^\circ$  South). Basic properties of the sample are presented in Table 2. The flux criterion was prompted by the sensitivity of TIMMI2 in spectroscopic mode which is  $\sim 100\text{mJy}/10\sigma$  in 1 hour. The sample is heterogenous with respect to the galaxy type: it contains six starbursts (SB), one HII, two Sy 1 and thirteen Sy 2. The distances range from 3.5–176 Mpc and the luminosities from  $0.7 - 120 \times 10^{10}L_\odot$ . Our TIMMI2 sample also contains sources lacking an ISO spectrum. These sources were selected from the Markarian catalogue (Markarian et al. 1989) to fill gaps in our primary observing schedule.

## 3. Observations

The N band imaging and spectroscopic observations were made with the TIMMI2 mid-infrared camera (Reimann et al. 2000, Käufel et al. 2003) at the ESO 3.6m telescope. The camera uses a  $240 \times 320$  pixel Raytheon Si:As array. In imaging we selected the  $0.2''$  pixel scale providing a total field of view of  $48'' \times 64''$ . For long-slit spectroscopy the resolving power is  $\Delta\lambda/\lambda \sim 400$  and we used the  $1.2''$  or  $3''$  slit and  $0.45''$  pixel field of view. Table 2 reports for each galaxy: observing date, total on-source integration time, filter and calibration standard. The filter is designated by

**Table 1.** A few parameters of our IRG sample. Velocities (col. 3) and distances (col. 4) are from NED. Col. 5 gives the linear size of  $1''$  at the distance  $D$ , and col. 6 the infrared luminosity.

Name	Type	v km/s	D Mpc	$1''$ pc	L $10^{10}L_\odot$
Centaurus A	Sy 2.0	547	3.5	17	0.68
Circinus	Sy 2.0	439	4	19	1.4
IC4329a	Sy 1.2	4813	65	315	7.6
IRAS05189–2524	Sy 2.0	12760	176	852	120
IRAS08007–6600	HII	12324	170	822	34
M83	SB	516	4	19	0.65
Mrk509	Sy 1.2	10312	141	684	14
Mrk1093	SB	4441	60	290	9.3
Mrk1466	SB	1327	18	87	0.7
NGC1068	Sy 2.0	1148	14	68	19
NGC1365	Sy 1.8	1636	22	106	8.3
NGC1386	Sy 2.0	868	18	87	0.71
NGC2966	SB	2044	27	131	1.1
NGC3256	SB	2738	37	178	35
NGC4388	Sy 2.0	2524	34	164	1.2
NGC5506	Sy 1.9	1853	25	120	2.3
NGC5643	Sy 2.0	1199	16	78	1.8
NGC6000	SB	2193	29	141	9.0
NGC6240	Sy 2.0	7339	100	483	60
NGC7552	SB	1585	21	102	9.8
NGC7582	Sy 2.0	1575	21	102	6.3
NGC7674	Sy 2.0	8671	118	573	31
PKS2048–57	Sy 2.0	3402	46	222	6.1

its central wavelength and the entry *grating* refers to 8–13  $\mu\text{m}$  spectroscopy.

Observations were performed in chopping and nodding mode with  $12''$  amplitude each with is a compromise between sensitivity and the ability to measure extended structures. To avoid saturation of the detector by the high ambient photon background the elementary integration times were typically 20 ms for imaging and 40 ms for spectroscopy. Elementary images were coadded in real time during the chopping cycles. Chopping was in North-South direction at a frequency of  $\sim 3\text{Hz}$ . After an interval of typically less than a few minutes the telescope was nodded in order to cancel the telescope emission and residuals in the sky subtraction. After coaddition of all chopping and nodding pairs there are two negative and one positive beam (slit) on the image which we combine applying a shift-and-add procedure. We note that TIMMI2 is not capable of measuring low surface brightness emission that is extended by more than half the chopping or nodding amplitude. Consequently, part of the diffuse emission is cancelled by the observing technique.

**Table 2.** Log of TIMMI2 Observations

Target	Date (2002)	Time (sec)	Filter ( $\mu\text{m}$ )	Calibrator
Centaurus A	Jan. 30	645	10.4	HD81420
	Jan. 30	3225	grating	HD81420
Circinus	Jan. 30	268	10.4	HD81420
	Jan. 30	967	grating	HD81420
IC4329A	Jan. 29	403	10.4	HD81420
	Jan. 29	2419	grating	HD81420
IRAS05189–2524	Feb. 01	361	8.6	HD32887
	Feb. 01	2257	grating	HD32887
	25.01.03	600	10.4	HD123139
	25.01.03	600	11.9	HD123139
IRAS08007–6600	Feb. 01	361	8.6	HD32887
	Feb. 01	469	11.9	HD32887
	Feb. 01	1935	grating	HD32887
	25.01.03	360	11.9	HD123139
M83	Jan. 30	322	10.4	HD81420
	Jan. 30	301	11.9	HD81420
	Jan. 30	2419	grating	HD81420
Mrk509	Jan. 30	322	10.4	HD81420
	Aug. 14	619	11.9	HD196171
	Aug. 14	619	11.9	HD196171
Mrk1093	Aug. 14	2580	grating	HD196171
	Feb. 02	602	11.9	HD32887
Mrk1466	Feb. 02	2903	grating	HD32887
	Feb. 04	903	8.6	HD123139
NGC1068	Feb. 02	903	11.9	HD123139
	Feb. 02	2419	grating	HD123139
	Jan. 29	268	10.4	HD32887
	Jan. 29	1209	grating	HD32887
NGC1365	Jan. 31	150	8.6	HD32887
	Jan. 31	604	grating	HD32887
	Jan. 30	645	10.4	HD32887
	Jan. 30	3225	grating	HD32887
NGC1386	Jan. 31	150	8.6	HD32887
	Jan. 31	1935	grating	HD32887
NGC2966	Aug. 15	619	11.9	HD1522
	Aug. 15	2580	grating	HD1522
NGC3256	Feb. 03	602	11.9	HD123139
	Jan. 31	180	8.6	HD123139
	Jan. 29	537	10.4	HD81420
	Jan. 29	3628	grating	HD81420
NGC4388	Jan. 31	3064	grating	HD123139
	Feb. 03	602	11.9	HD123139
	Feb. 03	2419	grating	HD123139
NGC5506	Feb. 02	602	11.9	HD123139
	Feb. 02	1612	grating	HD123139
NGC5643	Feb. 02	602	11.9	HD123139
	Feb. 02	1612	grating	HD123139
	Aug. 14	602	11.9	HD123139
	Aug. 14	1612	grating	HD123139
NGC6000	Jan. 29	215	10.4	HD123139
	Feb. 01	301	8.6	HD123139
	Feb. 01	2096	grating	HD123139
NGC6240	Aug. 13	619	11.9	HD123139
	Aug. 15	619	11.9	HD133774
	Aug. 13	3096	grating	HD123139
	Aug. 15	2580	grating	HD133774

**Table 2.** continued

Target	Date (2002)	Time (sec)	Filter ( $\mu\text{m}$ )	Calibrator
NGC7552	Aug. 15	929	11.9	HD1522
	Aug. 15	2580	grating	HD169916
	Aug. 15	3096	grating	HD1522
NGC7582	Aug. 14	619	11.9	HD178345
	Aug. 14	2580	grating	HD178345
	Aug. 14	2709	grating	HD1522
NGC7674	Aug. 15	619	11.9	HD178345
PKS2048–57	Aug. 14	619	11.9	HD178345
	Aug. 14	2460	grating	HD178345

TIMMI2 follow-up observations of ISO galaxies were obtained during January 28–February 3, August 13–14, 2002 and 4 photometric imaging observations on January 25, 2003. The observations of the targets were interleaved with those of nearby mid-infrared calibration standard stars, typically 4–5 of which were measured each night. Model spectra for the standards have an absolute photometric uncertainty of a few percent (Cohen et al. 1999). However, for stars of spectral type later than F there might be fundamental molecular lines present in the photospheric spectra, such as Si–O in the  $9\mu\text{m}$  region (Heras et al. 1998). These bands are not considered by the present photospheric models. Consequently, one must be careful not to over-interpret faint structures at these wavelengths. Furthermore close to the blue and red cut-off frequencies of the grating the terrestrial background varies strongly with ambient conditions and atmospheric corrections are more difficult. The same holds for wavelength regions of strong terrestrial lines near  $9.58\mu\text{m}$ ,  $11.73\mu\text{m}$  and  $12.55\mu\text{m}$ .

The N band imaging of the stars was performed in the same filter as the target and used for photometric flux conversion from photon count rates into astronomical units (mJy) and to establish the point spread function (PSF). The spectra of the stars were used for atmospheric corrections and for flux calibration of the target spectrum.

## 4. Data analysis

### 4.1. Mid-infrared imaging

We apply multi-aperture photometry on the shift-and-add processed image, which we refer to as raw or original image. For each aperture centred on the brightest pixel of the source we estimate the background as the mean flux derived in a 6 pixel wide annulus which is put 6 pixels away from the outer source aperture. The thus estimated aperture fluxes,  $F(r)$ , were plotted against the aperture radii,  $r$ , to provide the growth curve. The flux where the growth curve of the aperture photometry flattens was identified interactively and is taken as the total flux density. The

**Table 3.** Mid-infrared flux densities of TIMMI2 observations. Photometric uncertainty  $\sim 10\%$ .

Name	F(8.6) (Jy)	F(10.4) (Jy)	F(11.9) (Jy)
Centaurus A	-	0.65	-
Circinus	-	4.10	-
IC4329A	-	0.64	-
IRAS05189–2524	0.42	0.42	0.57
IRAS08007–6600	0.21	-	0.23
Mrk509	-	-	0.22
Mrk1093	-	-	0.16
Mrk1466	0.09	-	0.11
M83	-	0.11	0.23
NGC1068	14.8	17.6	-
NGC1365	0.40	0.46	-
NGC1386	-	-	0.40
NGC2966	-	-	<0.03
NGC3256	0.45	0.39	-
NGC4388	-	-	0.29
NGC5506	-	-	1.06
NGC5643	-	-	0.31
NGC6000	0.21	0.20	-
NGC6240	-	-	0.28
NGC7552	-	-	1.87
NGC7582	-	-	0.69
NGC7674	-	-	0.26
PKS2048–57	-	-	0.92

absolute photometric uncertainty is  $\sim 10\%$ . This error estimate is based on internal consistency of the calibration observations and monitoring of photometric calibration standard stars. We note that part of this error is due to large scale ( $\geq 10''$ ) sensitivity gradients on the detector array. Up to now no suitable flat fielding procedure has been established to further reduce the absolute photometric error.

The growth curve is used to extract spatial information. For example, if one calculates the growth curve of an Airy function up to its first dark ring then the aperture radius,  $r_{50\%}$ , where the flux is at 50% of its maximum value is half of the full width at half maximum (FWHM). Still the diffraction pattern of the telescope and the seeing has to be subtracted. If for an extended target one derives a 50% flux radius  $r_{50\%}^e$  and for a PSF a radius  $r_{50\%}^p$ , a size estimate of the source extension may be approximated by  $(r_{50\%}^o)^2 = (r_{50\%}^e)^2 - (r_{50\%}^p)^2$ . The size estimate by the growth curve depends on the total flux or a normalisation at large radii. Another diagnostic of the source extension is given by the differential flux profile, which is a function  $F(r_{i+i}) - F(r_i)$ , and as well difficult to normalise, this time at small radii. We take the sum of the aperture fluxes at  $r \leq r_{50\%}^o$ . With such normalisation the differential flux distribution of an extended target should be less steep than for the PSF.

The spatial resolution of the images are at best limited by the diffraction pattern of the 3.6m telescope, which provides a FWHM of  $0.7''$  at  $10\mu\text{m}$ . In order to increase the spatial resolution we applied a deconvolution procedure. We use the maximum entropy multi-resolution wavelet decomposition by Starck & Murtagh (2002). The gradient algorithm has been chosen with 4 wavelet scales assuming Gaussian distribution of the noise and we applied a  $5\sigma$  threshold, where  $\sigma$  is the noise as estimated on the object free part of the image. The method provides a residual map,  $R$ , which is a convolution of the deconvolved image,  $D$ , with the PSF,  $P$ , and subtracted from the original image,  $O$ ; symbolically:  $R = D * P - O$ . The iteration of the deconvolution is stopped so that the noise properties of the residual map is at similar level as the noise of the original image. However, for bright point-like sources with little extension we note that the residual map is polluted by the very bright central peak. Residuals are typically less than 5% of the peak flux of the deconvolved image. They are caused by finite sampling of a  $\delta$ -type function. From the growth curve of the deconvolved image we calculate its 50% flux radius,  $r_{50\%}^d$ . The residual map is used for error propagation.

To study the stability of the PSF and its influence on the deconvolution procedure, we calculate for each PSF the deconvolution and growth curves with any other PSF available of the same filter. For the deconvolved PSF images we find a mean size of  $\langle r_{50\%}^d \rangle = 0.098'' \pm 0.046''$ . Size estimates from the growth curves as measured on the raw images give a mean of  $\langle r_{50\%}^o \rangle = 0.224'' \pm 0.074''$ , which already closely matches the static aberration of the telescope. Altogether we verified that seeing in the mid IR gives only a small contribution to the PSF at the 3.6m. Nevertheless for deconvolution we apply the measured PSF matched closely in time to the target observation. A source is regarded to be unresolved if its radius measured on the raw and deconvolved image is below  $\langle r_{50\%}^o \rangle + 3\sigma(r_{50\%}^o)$ . Therefore, resolved sources have  $r_{50\%}^d > 0.24''$  and  $r_{50\%}^o > 0.44''$ , respectively. For galactic nuclei fulfilling these criteria, the differential source profile also shows signatures of extended emission.

Observed mid-infrared flux densities for the galactic nuclei are given in Table 3. For 10 out of 22 galaxies the nucleus is resolved. For these we show in Fig. 1–11 raw, PSF, deconvolved and residual maps and present growth curves as well as differential flux distributions. Absolute levels of the contours, shown on top of the gray scale images, can be derived together with Table 4, where we specify the peak flux densities of the raw and deconvolved images and the residual map. For the residual map we specify the  $1\sigma$  RMS noise level. The  $1\sigma$  RMS noise of the raw image is given in col. 3 of Table 5. It is an indicator of the sensitivity limit which we reached with TIMMI2.

Table 5 lists the central wavelength of the TIMMI2 filter (col. 2) together with the 50% flux radius,  $r_{50\%}$ , as derived from the raw (col. 4) and deconvolved (col. 5) image. The latter radius is our estimate of the source size (col. 6).

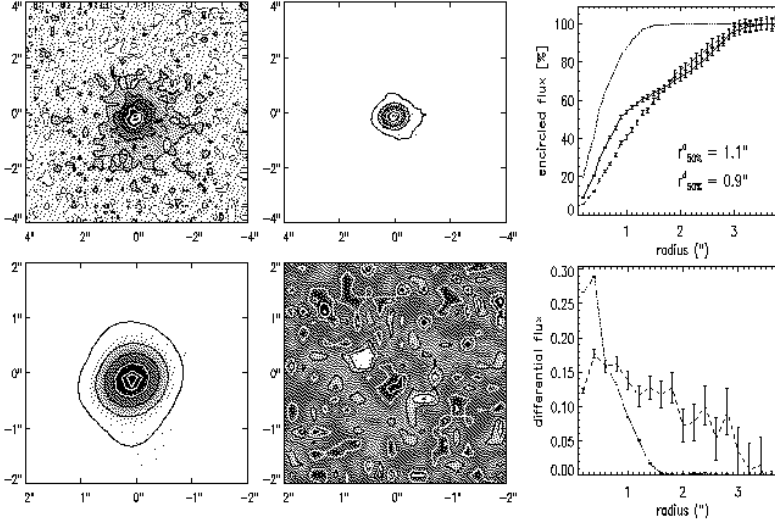


**Fig. 1.** NGC3256 at  $10.4 \mu\text{m}$ . On the raw (top-left), PSF (top-middle) and deconvolved image (bottom-left) contours are in black at 10%, 30% and 50% and in white at 75%, 90% and 95% levels of the peak flux; dotted contours are at  $-1\sigma$  and  $-3\sigma$  and dashed contours at  $+1\sigma$  and  $+3\sigma$ , respectively. On the residual map (bottom-middle) black contours are at  $-98\%$ ,  $-90\%$ ,  $-50\%$ , white contours at 50%, 90%, 98% of the peak. The peak fluxes and  $\sigma$  values are specified in Table 4. For all gray scale images North is up and East is left. Growth curves (top-right) and differential flux distributions (bottom-right) are shown for raw (dashed), PSF (dotted) and deconvolved image (full line). Error bars are  $1\sigma$  RMS.

**Fig. 2.** NGC7552 at  $11.9 \mu\text{m}$ , see Fig. 1. On the raw image (top-left), the PSF and the deconvolved image contours are set in black at 8%, 20% and 30% and in white at 50%, 75%, and 95% levels of the peak flux

**Fig. 3.** Mrk1093 at  $11.9 \mu\text{m}$ , see Fig. 1.

**Fig. 4.** Circinus at  $10.4 \mu\text{m}$ , see Fig. 1.

**Fig. 5.** Centaurus A at  $10.4 \mu\text{m}$ , see Fig. 1.

**Fig. 6.** NGC1068 at  $10.4 \mu\text{m}$ , see Fig. 1.

**Fig. 7.** NGC1386 at  $11.9 \mu\text{m}$ , see Fig. 1.

**Fig. 8.** NGC7582 at  $11.9 \mu\text{m}$ , see Fig. 1. On the raw image, the PSF and the deconvolved image contours are set in black at 14%, 20% and 50% and in white at 75%, 90%, and 95% levels of the peak flux, respectively.

**Fig. 9.** Mrk509 at  $11.9 \mu\text{m}$ , see Fig. 1.

**Table 4.** Peak surface brightness and RMS of nuclei with extended mid infrared emission.

Name	Raw Peak $\frac{\text{mJy}}{\text{arcsec}^2}$	Deconvolved Peak $\frac{\text{mJy}}{\text{arcsec}^2}$	Peak $\frac{\text{mJy}}{\text{arcsec}^2}$	Residual RMS $\frac{\text{mJy}}{\text{arcsec}^2}$
Centaurus A	881	2301	100	17
Circinus	3902	14806	167	31
Mrk509	637	10	2.6	0.4
Mrk1093	52	10	7.5	1.8
NGC1068	10078	31196	371	80
NGC1386	512	136	33	4.7
NGC3256	296	211	35	7.3
NGC6240	280	245	56	11
NGC7552	997	277	110	10
NGC7582	275	91	12	2.3
NGC7674	287	123	16	4.0

**Table 5.** Mid-infrared sizes of galactic nuclei.

1	2	3	4	5	6
Name	$\lambda$ $\mu\text{m}$	$\sigma^b$ $\frac{\text{mJy}}{\text{arcsec}^2}$	$r_{50\%}^o$ "	$r_{50\%}^d$ "	$r_{50\%}^d$ pc
Centaurus A	10.4	14	<0.37	<0.20	<3
Circinus	10.4	22	0.46	<0.20	<4
IC4329a	10.4	19	<0.28	<0.21	<66
IRAS05189–2524	8.6	18	<0.24	<0.20	<170
IRAS08007–6600	8.6	66	<0.23	<0.27	<222
Mrk509	11.9	10	1.2	2.4	1642
Mrk1093	11.9	13	1.9	1.69	490
NGC1068	8.6	48	0.53	0.27	18
NGC1068	10.4	18	0.58	0.35	24
NGC1365	8.6	64	<0.28	<0.35	<37
NGC1386	11.9	42	0.50	0.53	46
NGC3256	10.4	28	1.14	0.88	157
NGC4388	11.9	33	<0.30	<0.36	<59
NGC5506	11.9	22	<0.30	<0.20	<24
NGC6240	11.9	31	1.11	0.47	227
NGC7552	11.9	82	2.79	2.65	270
NGC7582	11.9	17	1.18	0.87	89
NGC7674	11.9	22	0.6	0.46	264
PKS2048–57	11.9	15	<0.2	<0.23	<51

<sup>b</sup>  $1\sigma$  RMS noise measured on the object-free part of the raw image.

<sup>o</sup> Mid-infrared radius where the flux is at 50% of the total as derived from the growth curves of the object (raw) and PSF images.

<sup>d</sup> Mid-infrared radius where the flux is at 50% of the total as derived from the growth curve of the deconvolved image.

**Fig. 10.** NGC6240 at  $11.9\ \mu\text{m}$ , see Fig. 1.**Fig. 11.** NGC7674 at  $11.9\ \mu\text{m}$ , see Fig. 1.

#### 4.2. TIMMI2 spectroscopy

The coaddition of all chopping and nodding pairs of raw frames in TIMMI2 spectroscopic observing mode gives two negative and one positive long-slit spectrum on the image. We developed an optimal extraction procedure for TIMMI2 spectra similar to Horne (1986): A source profile is extracted by collapsing the image along the dispersion direction and applying a median filter. Extension of the sources are considered to a  $2\sigma$  cut-off, where  $\sigma$  is calculated for each column in cross-dispersion direction and on the source free part of the array. Preliminary wavelength calibration is performed using tables provided by the instrument team. This calibration is fine tuned to sub-pixel accuracy by applying a linear wavelength shift. The shift is measured as an offset to atmospheric lines. The procedure is applied to the target and the calibration standard star. A division of both spectra removes the telluric lines. To minimise residuals of the sky line cancellation, we observed standard and target at similar airmasses. From the standard star spectrum we calculate the conversion factor from technical (ADU/s) into astronomical (Jy) units. The calibrated spectra are finally high-frequency noise filtered by the method described by Starck et al. (1997). Statistical errors are computed from unfiltered data. Because not all detector channels were always fully operational, the spectra of M83, CenA, Circinus, IC4329A, and NGC1068 could only be extracted long-ward of  $9\ \mu\text{m}$ .

#### 4.3. ISO spectroscopy

Whenever possible, we compare mid-infrared spectra at different spatial scales: high-resolution long-slit TIMMI2 spectroscopy ( $1'' - 3''$ ) and ISO spectra of much lower resolution ( $24'' \times 24''$  with ISOPHT, Lemke et al. 1996;  $14'' \times 20''$  with ISOSWS in the N band, de Graauw et al. 1996; and ISOCAM spectra which refer, unless otherwise stated, to the total emission of the galaxy, Cesarsky et al. 1996). The diffraction limits of the telescopes at  $10\ \mu\text{m}$  are:  $\sim 0.7''$  at the ESO 3.6m and  $\sim 8''$  with ISO.

For the brightest objects of our sample ISOSWS grating or line scans are reported by Thornley et al. (2000), Sturm et al. (2002) and Verma et al. (2003); ISOCAM spectra by Laurent et al. (2000), and ISOPHT spectra by Clavel et al. (2000), Laureijs et al. (2000), Rigopoulou et al. (1999), Siebenmorgen et al. (1999) and Spoon et al. (2002). For the remaining galaxies (Cen A, Circinus, IC 4329A, IRAS08007–6600, Mrk509, NGC1068, NGC1365, NGC1386, NGC3256, NGC4388, NGC5506, NGC5643, NGC6000, NGC6240, NGC7552, NGC7582) we extracted ISOPHT raw data from the ISO archive and reduced the spectra with standard routines of the ISOPHT interactive analysis system (PIA). Most

**Table 6.** Important features and lines between 8 to  $13\ \mu\text{m}$ .

Name	$\lambda^a$ $\mu\text{m}$	$I^b$ eV	Mode
PAH	8.6	–	C–H
Ar III	8.991	27.6	–
Mg VII	9.009	186.5	–
Fe VII	9.537	99.1	–
H <sub>2</sub> 0-0 S(3)	9.660	–	–
Silicate	9.7	–	Si–O
S IV	10.511	34.8	–
PAH	11.3	–	C–H
Ne II	12.814	21.6	–
PAH	12.7	–	C–H

<sup>a</sup> Rest wavelength.

<sup>b</sup> Ionisation energy with respect to the next lower ionisation level.

of the ISOPHT spectra appear for the first time in the refereed literature.

## 5. Results

Here we present our high resolution mid-infrared imaging and spectroscopy data using TIMMI2 together with the low resolution ISO spectra. The data of the individual objects are briefly discussed and whenever necessary compared to observations available at other wavelengths. We will first describe the starbursts and then the Seyferts.

A variety of broad band dust features and fine structure lines fall within the N band; they are summarised in Table 6. Gas emission lines imply either the presence of ionising shocks (Contini & Contini 2003) or a hard photon flux. For ionisation potential below  $\sim 50\text{eV}$ , photo-ionisation by hot stars is the most likely explanation for the excitation mechanism. In the  $8\text{--}13\ \mu\text{m}$  spectral range there are no lines which require very hard radiation only produced by AGNs ( $> 200\text{eV}$ ). At the resolving power of TIMMI2 ( $\Delta\lambda/\lambda \sim 400$ ) the lines are generally unresolved. The [Ar III] and [Mg VII] line occur at the same wavelength but their excitation requirements are very different. The [Fe VII] line may be blended by the Ozone band, [S IV] is in a clean atmospheric region. The PAH band emission at  $12.7\ \mu\text{m}$  is close to the [Ne II] at  $12.8\ \mu\text{m}$ .

However, as we will demonstrate by model calculations in Sect. 7, detection or non-detection of PAH features can serve as a diagnostic tool to distinguish the dominating excitation within the nucleus: starbursts or AGN; although the dividing line is not sharp. The mid IR spectra of spirals show dust continuum and strong PAH bands. Close to massive stars there is additional hot dust continuum emission and some photo-destruction of PAH (Siebenmorgen 1993). So that starburst galaxies still show PAH bands but at lower PAH band-to-continuum ratios than observed in spirals. In the harsh environment close to an AGN one expects much lower PAH band-to-continuum ratios than in

starbursts and most often PAH bands are absent. In the immediate environment of the hard X-ray and intense UV radiation of an AGN the PAH get destroyed. In addition significant emission by hot dust from the inner torus wall of the unified model is expected which further decreases the PAH band-to-continuum ratios.

The silicate band if present in the galactic nuclei is seen so far only in absorption. From its depth one can estimate the visual extinction. We apply  $\tau_V \sim 18 \cdot \tau_{9.7\mu\text{m}}$ . However,  $\tau_{9.7\mu\text{m}}$  is difficult to estimate without detailed model calculations of the PAH contribution to the mid-infrared continuum (Siebenmorgen et al. 2001). Whenever possible we interpolate a line to the spectra from  $\sim 8$  to  $11 \mu\text{m}$  and so derive a crude estimate of  $\tau_{9.7\mu\text{m}}$  and the total visual extinction. This procedure maybe uncertain within a factor 2.

## 5.1. Starburst galaxies: imaging and spectroscopy

### 5.1.1. NGC6000

ISO observations and radiative transfer models for the dust in NGC 6000 are presented by Siebenmorgen et al. (1999). At  $12\mu\text{m}$ , the flux from IRAS is stronger than from ISOPHT which suggests that the mid IR source is extended beyond  $24''$ . TIMMI2 images at  $8.6$  and  $10.4\mu\text{m}$  are fuzzy, without a point source. Both spectra in Fig. 12 are dominated by PAH emission. In the TIMMI2 spectrum, the  $11.3\mu\text{m}$  PAH band-to-continuum ratio is about two times smaller (Table 8). The [Ne II] line is detected, but the  $12.7\mu\text{m}$  PAH band is seen only marginally. We estimate from the depth of the silicate absorption in the ISOPHT (TIMMI2) spectrum a visual extinction of  $\sim 25$  mag (20 mag); both values are consistent with  $A_V = 29$  mag inferred from the radiative transfer models.

### 5.1.2. Mrk1466

The signal-to-noise in the TIMMI2 image is low, hence we cannot determine the source size. The only feature in the TIMMI2 spectrum detected at high confidence is the  $11.3\mu\text{m}$  PAH band (Fig. 12 and Table 8). ISO spectra are not available for comparison.

### 5.1.3. NGC3256

The brightness in the TIMMI2 image increases towards the center. The emission is resolved and there is no point source in the core (Fig. 1). Both ISOPHT and TIMMI2 spectra are dominated by PAH emission (Fig. 12). The  $11.3\mu\text{m}$  PAH band-to-continuum ratio is lower in the smaller aperture spectrum by about a factor 2 (Table 8). There is strong [Ne II] emission (Table 7). Due to the  $8.6\mu\text{m}$  PAH band and because the atmospheric ozone band at  $\sim 9.5\mu\text{m}$  has not been fully eliminated, it is difficult to say whether there is silicate absorption at all.

**Fig. 13.** Mid-infrared flux densities (in Jy) of M83: Data presented are: ISOPHT ( $24''$  aperture, histogram), TIMMI2 spectroscopy ( $3''$ , full line) with  $3\sigma$  errors (shadow) and TIMMI2 photometry with  $1\sigma$  error bars (Table 3). For comparison we show the spectrum of the Galactic Center (dashed).

### 5.1.4. NGC7552

The deconvolved  $11.9\mu\text{m}$  TIMMI2 image at  $0.45''$  angular resolution (Fig. 2) shows four hot spots, equidistant from the center, that form a ringlike circumnuclear starburst. Two of the hot spots have already been detected by Schinnerer et al. (1997) in their  $10.5\mu\text{m}$  map with  $0.8''$  resolution. These authors also present near infrared images and spectral synthesis models consistent with the idea of a starburst ring. The slit during the TIMMI2 grating observations was positioned at the brightest knot,  $\sim 3''$  North of the centre; the [Ne II] line is visible as well as the  $11.3\mu\text{m}$  PAH band (Table 7). The ISOPHT spectrum shows the [Ar II] line and strong PAH emission. The  $11.3\mu\text{m}$  PAH band-to-continuum ratio is a factor  $\sim 3$  lower in the smaller aperture spectrum (Table 8). Silicate absorption is weak in both spectra, it corresponds to  $A_V \sim 3$  mag (Fig. 12).

### 5.1.5. Mrk1093

The source at  $11.9\mu\text{m}$  is extended in the East-West direction (Fig. 3). TIMMI2 spectroscopy (Fig. 12) reveals the [Ne II] line and PAH bands at  $8.6$  and  $11.3 \mu\text{m}$ . ISO spectra are not available for comparison.

### 5.1.6. IRAS08007–6600

This is one of the most distant galaxy in our sample ( $170$  Mpc). The TIMMI2 images at  $8.6 \mu\text{m}$  and  $11.9 \mu\text{m}$  are unresolved. The energy distribution peaks near  $60\mu\text{m}$  (Vader et al. 1993). The TIMMI2 spectrum does not show evidence for the presence of  $8.6 \mu\text{m}$  PAH emission. This feature is, however, present in the larger aperture ISOPHT spectrum (Laureijs et al. 2000). The absence may be due to low signal-to-noise of our TIMMI2 spectrum. The silicate absorption is weak and indicates  $A_V \sim 6$  mag from the central  $200\text{pc}$  (Table 5).

### 5.1.7. M83

M83 is the nearest starburst galaxy in our sample. TIMMI2 images at  $10.4$  and  $11.9 \mu\text{m}$  show a fuzzy structure without striking point sources. As typical for starburst galaxies, the large aperture ISOPHT spectrum is dominated by PAH emission bands. In contrast, the TIMMI2 spectrum of the central  $60\text{pc}$  does not show any sign of PAH emission features and is dominated instead by a smooth continuum with a weak [Ne II] emission line (Fig. 13). The shape of the continuum is consistent with

**Fig. 12.** Mid-infrared flux densities (in Jy) of *starburst* galaxies: Data presented are: ISOPHT (24'' aperture, histogram), TIMMI2 spectroscopy (3'', full line) with  $3\sigma$  errors (shadow) and TIMMI2 photometry with  $1\sigma$  error bars (Table 3).

**Table 7.** Integrated atomic line fluxes and  $3\sigma$  upper limits ( $10^{-20}\text{W}/\text{cm}^2$ ) of TIMMI2 and ISOSWS spectra.

Name	[S IV]	[S IV]	[Ne II]	[Ne II]
Aperture	3''	14'' × 20''	3''	14'' × 27''
Centaurus A	<2.4	1.4 <sup>b</sup>	22.6 ± 1.4	22.1 <sup>b</sup>
Circinus	<3.6	12.7 <sup>b</sup>	6.6 ± 0.9	90 <sup>b</sup>
IRAS05189+2524	<1.7			
IRAS08007-6600	<1.2			
IC4329a	1.8 ± 0.5		1.6 ± 0.3	
M83	<0.3		1.7 ± 0.2	
Mrk1093	<2.2		3.0 ± 0.5	
Mrk1466	<1.8		<2.3	
Mrk509	<1.3		<1.3	1.3 <sup>b</sup>
NGC 1068	30.1 ± 6.2	58 <sup>b</sup>	<14.2	70 <sup>b</sup>
NGC 1365	<1.7	2.6 <sup>b</sup>	<1.8	40.9 <sup>b</sup>
NGC 1386	<2.8		<2.8	
NGC 3256	<1.6	0.9 <sup>c</sup>	28.5 ± 1.0	89.2 <sup>c</sup>
NGC 4388	3.4 ± 0.9		5.4 ± 0.9	
NGC 5506	3.5 ± 0.9	5.4 <sup>b</sup>	2.9 ± 0.9	5.9 <sup>b</sup>
NGC 5643	<1.3		1.6 ± 0.4	
NGC 6000	<2.0		15.1 ± 1.1	
NGC 6240	<1.4		5.0 ± 1.6	17 <sup>a</sup>
NGC 7552	<8.3	0.3 <sup>c</sup>	49.0 ± 5.6	68 <sup>c</sup>
NGC 7582 (1.2'')	<3.7	1.8 <sup>b</sup>	<8.8	14.8 <sup>b</sup>
NGC 7582 (3.0'')	<1.6	1.8 <sup>b</sup>	8.9 ± 1.2	14.8 <sup>b</sup>
PKS2048-57	<2.7		<3.6	2.1 <sup>b</sup>

<sup>a</sup> Thornley et al. (2000), <sup>b</sup> Sturm et al (2002), <sup>c</sup> Verma et al. (2003)

the profile of the silicate absorption feature as found towards the ISOSWS position Sgr A\* in the Galactic center (Lutz 1999). Given their similarity, we speculate that the conditions in the nucleus of M83 may be similar to those in the Galactic center. In the latter, PAHs are thought to be destroyed by the local intense radiation field ( $\sim 10^{6.5} \times \text{ISRF}$ ) contributed by massive stars found in the Galactic center (Lutz 1999). Indeed far infrared spectroscopic images of fine structures lines in M83 indicate a strong central starburst activity headed by O9 stars (Stacey et al. 1998). So that this is our best example where PAH destruction occurs by the strength of the radiation field rather than by its hardness. The latter process is discussed in Sect. 6. From the depth of the silicate feature we estimate a visual extinction  $\sim 20\text{mag}$ .

## 5.2. Seyfert galaxies: imaging and spectroscopy

### 5.2.1. Circinus

Circinus is the closest galaxy of our sample that contains an obscured Seyfert nucleus. In the TIMMI2  $10.4\mu\text{m}$  image (Fig. 4), half the flux comes from an unresolved core, the other half from a 1''-sized blob elongated North-South. At a comparable scale, resolved emission at  $8.5\mu\text{m}$  is reported by Siebenmorgen et al. (1997). The photometry of ISOPHT (this work) and ISOSWS (Moorwood et al. 1996) give similar fluxes for  $\lambda > 9\mu\text{m}$ , but ISOSWS is systematically weaker 20%–30% between 6 –  $9\mu\text{m}$ . From the silicate absorption feature we estimate a visual extinction  $A_V > 15\text{mag}$ .

In the large aperture ISOSWS spectrum, one sees the silicate absorption feature, strong line emission ([S IV], [Ne II]) and PAH bands. In the TIMMI2 spectrum, [S IV] and [Ne II] are not detected so they cannot be of nuclear origin. The TIMMI2 absolute fluxes agree well with Roche et al. (1991) made with a 5'' aperture.



**Fig. 14.** Mid-infrared flux densities (in Jy) of *Seyfert* galaxies: Data presented are: ISOPHT (24'' aperture, histogram), ISOCAM (total field or nuclear spectrum, dashed), ISOSWS (14~20'', dotted), UCL (5'', diamonds), TIMMI2 spectroscopy (3'', full line) with 3 $\sigma$  errors (shadow) and TIMMI2 photometry with 1 $\sigma$  error bars (Table 3).

Moorwood & Oliver (1994) find that the central 6pc region is dominated by an AGN whereas star formation, as traced by H $\alpha$  and Br $\gamma$  recombination lines, occurs in Circinus in a (partial) ring of 200pc radius. This ring lies outside our map of Fig. 3. Model calculations of the dust re-processing of the AGN are presented by Siebenmorgen et al. (1997) and Ruiz et al. (2001).

Generally speaking, when one observes a Sy1 galaxy with a large aperture, one has a free view to the inner wall of the torus and detects strong mid-infrared emission from hot (large) grains. The PAH band-to-continuum ratio is then relatively low. In a Sy2, like Circinus, the inner torus is obscured and hence, the hot grains are invisible and the PAH band-to-continuum ratio is higher. This picture is supported in the case of Circinus, but also for Sy1 and other Sy2 galaxies (see below).

### 5.2.2. Centaurus A

This is the closest example of an AGN in our sample. In the TIMMI2 image it shows an unresolved core of less than 0.5'' (Fig. 5). The raw image and the growth curve (Fig. 5) indicate weak extended emission over  $\sim 2''$  with a surface brightness ten times lower than at the peak. The ISOCAM (Laurent et al. 2000) and ISOPHT (this work) spectra are PAH dominated whereas the TIMMI2 spectrum is featureless except for the presence of a strong [Ne II] line (Fig. 14). The visual extinction estimated from the silicate absorption detected in the ISOPHT and TIMMI2 spectra is around 14 mag.

### 5.2.3. NGC1068

TIMMI2 resolves the nucleus of this prototype Sy2 galaxy (Fig. 6) and our image of the core agrees with the long integrations by Alloin et al. (2000) using CAMIRAS and Bock et al. (2000) with MERLIN at Keck. However, we are not sensitive enough to confirm the individual hot cores found in those maps. PAHs are detected in the integrated ISOCAM (Laurent et al. 2000) and in our ISOPHT spectrum, but in a smaller aperture they disappear (Fig. 14, see also the ISOSWS spectrum of Lutz et al. 2000). The continuum is of similar strength for ISOSWS and TIMMI2 indicating that the AGN is indeed the major source in the central 1kpc region.

The ISOCAM spectrum of the central 9'' by Laurent et al. (2000) is, like ISOSWS and TIMMI2, free of PAHs. The [Ne II] line is absent in TIMMI2, but strong in the ISOSWS spectrum, [S IV] is seen in both. The strength of the silicate absorption band increases with spatial resolution; for the central 20pc, we estimate  $A_V \geq 5$  mag.

### 5.2.4. NGC5643

This Sy2 galaxy shows high-excitation optical lines (Kinney et al. 1993). The emission in [O III] and H $\alpha$  is extended up to  $\sim 20''$  (Schmitt et al. 1994). The 11.9 $\mu$ m TIMMI2 image is fuzzy, without a point source. The [Ne II] line is detected by TIMMI2 and for the [S IV] line we get an upper limit (Table 7). PAHs are strong in the ISOPHT aperture, whether they are seen with TIMMI2 is unclear (Fig. 14).

### 5.2.5. NGC1386

The TIMMI2 image of this Sy2 galaxy (Ferruit et al. 2000) has an unresolved core (Table 5) and an extended component (Fig. 7). The ISOPHT spectrum shows PAH bands and tentative, weak silicate absorption. In the TIMMI2 spectrum, (Fig. 14) one sees the silicate feature, corresponding to  $A_V \approx 30$  mag, but no PAHs.

### 5.2.6. NGC1365

A face-on Sy1 galaxy with an unresolved core in the TIMMI2 image. Its mid-infrared emission is dominated by PAHs everywhere except in the very center. The band-to-continuum ratio decreases with decreasing aperture size (Fig. 14). PAH bands are not present in the TIMMI2 spectrum (Table 8). [S IV] and [Ne II] emission is detected only with ISOSWS, but not with TIMMI2. The TIMMI2 continuum is flat without evidence of silicate absorption.

### 5.2.7. NGC4388

A galaxy with a Sy2 nucleus where Ho & Ulvestad (2001) see at radio wavelengths two components, 1.9'' (150 pc) apart, none of them coincides with the position of the optical peak. A hard X-ray peak is found at the position of the active nucleus (Iwasawa et al. 2003). As in the previous examples, the TIMMI2 image has a single unresolved core (Table 5), and there are strong PAH bands in the ISOPHT, but none in the TIMMI2 spectrum (Fig. 14). The [S IV] and [Ne II] lines are detected with TIMMI2 (Table 7).

### 5.2.8. IRAS05189–2524

In this most distant object of our sample, the central source in the TIMMI2 image is unresolved (Table 5). The same conclusion was reached by Soifer et al. (2000) using MERLIN at Keck. ISOPHT sees weak PAH emission (Laureijs et al. 2000) and an absorption feature at 6 $\mu$ m attributed to water ice (Spoon et al. 2002). PAH bands (Fig. 14) as well as gas emission lines are absent in the

**Fig. 15.** Mid-infrared flux densities (in Jy) of *Seyfert* galaxies: Data presented are: ISOPHT (24'' aperture, histogram), TIMMI2 spectroscopy (3'', full line and 1.2'' dotted) with  $3\sigma$  errors (shadow) and TIMMI2 photometry with  $1\sigma$  error bars (Table 3).

TIMMI2 spectrum. From the silicate absorption, we estimate  $A_V \sim 12$  mag.

### 5.2.9. NGC7582

The spectrum is a superposition of a Sy2 nucleus and a starburst (Storchi-Bergmann et al. 2000). The AGN is responsible for X-ray emission over a few kpc (Levenson et al. 2000). Optical and near IR images (Regan & Mulchaey 1999) indicate a complex dust morphology. There is a lane that runs from the southeast to an absorbing ring north of the chain of blue clumps; the TIMMI2 image reflects this structure (Fig. 8). PAH bands are detected with ISOPHT, but not [S IV]. The excellent seeing conditions during the TIMMI2 observations allowed us to use besides the 3'' also the 1.2'' slit. The spectra look quite similar at both resolutions (Fig. 15): [Ne II] is present, the PAH band is detected at  $11.3\mu\text{m}$  but not at  $8.6\mu\text{m}$ . From the silicate absorption we estimate  $A_V \sim 20$  mag. The  $11.3\mu\text{m}$  PAH band-to-continuum ratio is in TIMMI2 lower than in ISOPHT by about a factor 6 (Table 8).

### 5.2.10. NGC5506

The optical spectrum of this Sy2 galaxy is comparable to what one finds in young starburst galaxies, however, the high excitation lines ([Ne V], [Fe VII], [He II]) mandate the presence of a non-thermal continuum (Oliva et al. 1999). The X-ray spectrum is highly absorbed (Pfefferkorn et al. 2001). In the  $8\text{--}13\mu\text{m}$  wavelength range, [Ar III]/[Mg VII], [S IV] and [Ne II] emission lines are detected with ISOSWS, [S IV] and [Ne II] lines at similar strengths with TIMMI2 (Table 7). Evidence of PAH emission is found in the ISOPHT spectrum at  $6.2\mu\text{m}$  (Rigopoulou et al. 1999), whereas TIMMI2 sees a featureless spectrum. TIMMI2 and ISOPHT agree very well photometrically (Fig. 15). We estimate an optical depth of over 15 mag towards the core.

### 5.2.11. PKS2048–57

In the near-infrared, the nuclear source of this object is very red ( $K-L = 2.1$  mag) and heavily polarised (17%) which is explained by a non-thermal contribution (Hough et al. 1987). Its spectral energy distributions peaks at  $60\mu\text{m}$  (Hessler & Vader 1995) and the radio power is 2 orders of magnitude greater than that of typical Seyferts. The mid IR image is dominated by an unresolved core. The ISOPHT spectrum shows weak PAH emission. The TIMMI2 spectrum is badly affected by telluric sampling noise and no PAH features are visible. [Ne II] and

[Ar III]/[Mg VII] is detected by ISOSWS but not with TIMMI2.

### 5.2.12. IC4329A

This Sy1 galaxy is point-like in our TIMMI2 images, but shows extended [O III] and  $H\alpha$  emission (Mulchaey et al. 1996). The TIMMI2 and ISOPHT spectra appear to trace the same components, except for the [S IV] line which is stronger in the large aperture (Fig. 15). [Ne II] is seen with TIMMI2; the feature near  $9.4\mu\text{m}$  is probably telluric.

### 5.2.13. Mrk509

The emission of this Sy1 galaxy is at  $11.9\mu\text{m}$  dominated by an unresolved core and marginal resolved emission below the 10% level of the peak flux (Table 4) is found toward the South-East (Fig. 9). This may be supported by the slight increase of the mid-infrared emission in the larger ISOPHT aperture as compared to the TIMMI2 spectrum (Fig. 15). Source extension towards the south is also reported by near infrared observations (Winge et al. 2000). The ISOPHT spectrum is typical for a Sy1 (Clavel et al. 2000), it shows weak PAH emission over a strong continuum. In the TIMMI2 spectrum PAH bands are not detected (Table 8). Both spectra do not show evidence of silicate absorption. [Ne II] is detected by ISOSWS but not with TIMMI2.

### 5.2.14. NGC6240

A famous ultraluminous merger with a deeply hidden AGN. The AGN reveals itself by the strong iron line at 6.4 keV and the powerful continuum at 100 keV (Matt et al. 2000). Two hard X-ray nuclei have been recently detected by Komossa et al. (2003). Near infrared spectra indicate very low metallicity ( $\sim 1/10$  solar, Oliva & Origlia 1998). NICMOS images (Scoville et al. 2000) show two nuclei separated by  $1.6''$  (0.8 kpc) North-South. There are also two nuclei at radio wavelengths  $1.4''$  apart (Condon et al. 1996), the CO (2-1) peak lies in between (Tacconi et al. 1999). The TIMMI2 image at  $11.9\mu\text{m}$  (Fig. 8) reveals the nuclear region to be dominated by a strong core, which we identify with the Southern nucleus (Tecza et al. 2000). A fainter structure, at 10% of the peak flux of the core, extends  $\sim 2''$  to the North and matches the structure observed at lower resolution at near-infrared wavelengths (Tecza et al. 2000).

The ISOPHT spectrum is dominated by strong PAH emission and shows in addition emission lines of [Ar II],  $H_2$  0-0 S(5) (blended with [Ar II]) and  $H_2$  0-0 S(3).

**Table 8.** Continuum subtracted  $11.3\mu\text{m}$  PAH band fluxes,  $F$ , (in  $10^{-20}\text{W}/\text{cm}^2$ ) and PAH band-to-continuum ratios,  $R$ , of the TIMMI2 ( $3''$  slit) and ISOPHT ( $24''$  aperture) spectra.

Name	$F^{\text{TIMMI2}}$	$R^{\text{TIMMI2}}$	$F^{\text{ISO}}$	$R^{\text{ISO}}$
Circinus	<50	< 0.1	530	0.4
Centaurus A	<11	< 0.1	100	0.9
IC4329a	< 6	< 0.1	<10	<0.1
IRAS05189+2524	<10	< 0.1	< 3	<0.1
IRAS08007–6600	<6	< 0.1	<10	<0.1
M83	< 2	< 0.1	252	1.2
Mrk509	< 7	< 0.1	17	0.1
Mrk1093	10	1.0	–	–
Mrk1466	4	1.1	–	–
NGC 1068	<95	< 0.1	<750	<0.1
NGC 1365	<11	0.2	125	0.6
NGC 1386	<16	< 0.1	165	0.6
NGC 3256	30	0.4	107	1.0
NGC 4388	<11	< 0.2	17	0.6
NGC 5506	<16	< 0.1	<15	<0.1
NGC 5643	<10	0.2	20	0.5
NGC 6000	16	0.6	67	1.1
NGC 6240	12	0.6	21	1.0
NGC 7552	33	0.3	162	0.9
NGC 7582	19	0.2	110	1.3
PKS2048–57	<22	< 0.1	<50	<0.1

Interestingly, the latter line is absent in our TIMMI2 spectrum. Most of the [Ne II] emission ( $\sim 2/3$ ) originates from outside the  $3''$  slit (see Table 7). Both spectra (Fig. 15) show prominent PAH emission. The  $8.6\mu\text{m}/7.7\mu\text{m}$  band ratio is small in ISOPHT and the PAH band at  $8.6\mu\text{m}$  feature is not even detected with TIMMI2. Between 9 and  $10.5\mu\text{m}$  the TIMMI2 spectrum is noise dominated. The silicate absorption, as of ISOPHT suggests  $A_V > 25$  mag.

### 5.2.15. NGC7674

This Sy2 is slightly extended in the radio and has within  $0.5''$  a double source (Kukula et al. 1995). The deconvolved  $11.9\mu\text{m}$  TIMMI2 image is also extended and at  $0.5''$  (Fig. 11, Table 5) dominated by a single core. Previous mid IR maps by Miles et al. (1996) have insufficient resolution to resolve the galaxy but their absolute photometry is consistent with ours. The  $5''$  resolution UCL spectrum (Roche et al. 1991) is rather featureless, whereas the ISOPHT spectrum contains several PAH bands (Schulz, priv. communication). We could not yet perform TIMMI2 spectroscopy.

## 6. Heating and evaporation of PAHs

We discuss the survival of PAHs in starburst and AGN environments with energetic photons of, at least, a few

**Fig. 16.** The absorption efficiency of a graphite sphere of  $10\text{\AA}$  radius. Mie theory is still assumed to be valid at X-rays. Optical constants from Laor & Draine (1993).

hundred eV. Such photons can only be emitted by an X-ray source.

### 6.1. The evaporation condition

Let  $P(T)$  be the temperature distribution of an ensemble of very small grains, for example, PAHs, so that  $P(T) dT$  gives the probability of finding a particular grain in the temperature interval  $dT$  around  $T$ . Whereas grain cooling usually proceeds through emission of infrared photons, in a very hot particle, above  $\sim 2500\text{K}$ , evaporation is more effective (see Fig. 8 of Voit, 1991). The evaporation rate is proportional to the number of surface atoms,  $N_{\text{surf}}$ , for which approximately  $N_{\text{surf}} \sim N^{2/3}$  if  $N$  is the total number of atoms in the grain.

Let  $P_1$  and  $P_2$  be the probabilities that a surface atom is at an energy level below or above the binding energy  $E_b$ , respectively. Usually,  $P_2 \ll 1$ , so  $P_1 \simeq 1$ , and obviously  $P_1 + P_2 = 1$ . For a Boltzmann distribution,  $P_2/P_1 \sim \exp(-E_b/kT)$ . Due to phonon collisions, an atom changes its level at a rate given by the Debye frequency  $\nu_D$ . In one second, the atom is  $P_2\nu_D$  times above  $E_b$ , the evaporation rate is therefore

$$R_{\text{ev}} = N_{\text{surf}} \nu_D e^{-E_b/kT} . \quad (1)$$

Evaporation rises exponentially with temperature. To counterbalance it, atoms must be built into the grain. The rate at which this occurs is proportional to the thermal velocity of atoms, or to  $T^{1/2}$ , and to the density of the interstellar medium. The exponential process of evaporation wins over accretion by orders of magnitude in a fairly narrow range of  $T$ , the density is not relevant. Let us assume that the grains evaporate if a certain fraction of them,  $f_{\text{ev}}$ , is above some critical temperature  $T_{\text{cr}}$ . The latter should be somewhat greater than  $T_{\text{ev}}$ . Relegating all complicated or unknown physics to the parameters  $f_{\text{ev}}$  and  $T_{\text{cr}}$ , we write the condition for evaporation as

$$I_{\text{ev}} \equiv \int_{T_{\text{cr}}}^{\infty} P(T) dT > f_{\text{ev}} . \quad (2)$$

Reasonable numbers for  $T_{\text{cr}}$  in (2) are  $2500\text{K}$  and  $f_{\text{ev}} \sim 10^{-8}$ , but such suggestions do, of course, not constitute a theory.

### 6.2. X-ray cross sections for dust absorption

An AGN differs from a starburst nucleus of the same bolometric luminosity by the hardness of its radiation field. We are here interested in the question how the presence of very energetic photons in AGNs affects the chance of survival of small grains. First, we remark briefly on the X-ray absorption cross section of dust.

**Fig. 17.** The distribution function of the temperature,  $P(T)$ , for graphite grains of  $5\text{\AA}$  radius. Monochromatic flux  $F = 10^4 \text{ erg cm}^{-2} \text{ s}^{-1}$ , photon energies from 10 to 80eV.

When a grain absorbs an optical or UV photon of frequency  $\nu$ , its internal energy rises by the full amount  $h\nu$ . Furthermore, when the grain is not smaller than the wavelength, the absorption efficiency is approximately one. The situation is different at X-rays. The interaction of hard photons with interstellar dust and the limits of Mie theory have been studied by Voit (1991), Laor & Draine (1993) and Dwek & Smith (1996). Below 10keV, the main absorption process is photo-ionization of inner atomic shells. The excited electron loses energy in inelastic scattering as it travels through the grain, but may also leave the grain and carry away kinetic energy as a photo-electron. When an X-ray photon has created a gap in the innermost shell, the gap will be filled by a downward transition of an electron from an upper shell and the energy may escape either as a photon, or non-radiatively through ejection of an Auger electron.

The computations of Dwek & Smith (1996) indicate that for graphite particles of  $50\text{\AA}$  radius, soft X-ray photons with  $h\nu \lesssim 100 \text{ eV}$  deposit practically all their energy in the grain and Mie theory is still valid. For photon energies above  $h\nu = 100 \text{ eV}$  and particle radii  $a < 50\text{\AA}$ , only part of the photon energy is deposited in the grain and we therefore reduce the absorption efficiency by a factor  $\propto 1/\nu$ .

Fig. 16 illustrates the absorption efficiency,  $Q^{\text{abs}}$ , from Mie theory of graphite grains with radii from 10 to  $1000\text{\AA}$  (see Fig. 2 of Laor & Draine (1993) for a wider range of parameters). The jump at  $43\text{\AA}$  (290eV) is due to the ionization threshold of the K-shell of the carbon atoms. At still higher frequencies, one has the typical  $\nu^{-3}$  cross section for ionizing solitary atoms. The drop in  $Q^{\text{abs}}$  at wavelengths short of the first ionization level at  $\sim 10 \text{ eV}$  is less steep ( $Q^{\text{abs}} \propto \nu^{-2}$  for  $a \leq 100\text{\AA}$ ); for big grains ( $a > 1000\text{\AA}$ ),  $Q^{\text{abs}}$  is essentially flat at these wavelengths.

When, as for X-rays, absorption is due to the excitation of inner atomic shells, the cross section of a grain,  $K^{\text{abs}}$ , depends only weakly on the way the atoms are held together in the solid. One can therefore roughly set  $K^{\text{abs}}$  proportional to the number of atoms in the grain. The dust particle in Fig. 16 with  $10\text{\AA}$  radius consists of  $N_{\text{C}} = 520$  carbon atoms and has  $Q^{\text{abs}} \simeq 0.2$  in the interval  $10 \text{ eV} \leq h\nu \leq 20 \text{ eV}$ , and  $Q^{\text{abs}} \propto \nu^{-2.2}$  for  $h\nu > 20 \text{ eV}$ . For the cross section per carbon atom,  $C^{\text{abs}}$ , this implies  $C^{\text{abs}} \simeq 10^{-17} \text{ cm}^2$  for  $10 \text{ eV} \leq h\nu \leq 20 \text{ eV}$ , and  $C^{\text{abs}} \simeq 10^{-17} \times (20/h\nu)^{2.2} \text{ cm}^2$  for  $h\nu > 20 \text{ eV}$ . We will use these crude numbers to calculate the cross section of PAHs.

**Fig. 18.** The fraction of graphite grains of  $5\text{\AA}$  (solid lines) and  $10\text{\AA}$  (dashed lines) radius above a critical temperature  $T_{\text{cr}} = 2500 \text{ K}$  (see Equation 2). The strength of the monochromatic flux  $F$  is indicated.

**Fig. 19.** The fraction of PAHs with  $N_{\text{C}} = 100$  carbon atoms above a critical temperature  $T_{\text{cr}} = 2500 \text{ K}$  (see Equation 2). The strength of the monochromatic flux  $F$  is indicated.

### 6.3. The temperature distribution of PAHs in a hard radiation field

To investigate how the distribution function  $P(T)$  and, in particular, the evaporation condition (2) depend on the photon energy, we consider a source with a monochromatic flux of strength  $F$ , all photons have then the same energy  $h\nu$ . While keeping the value of the flux fixed, we change  $h\nu$ , so if  $N_{\text{ph}}$  is the number of photons,  $N_{\text{ph}}h\nu = F$  stays constant. Low energy photons impinge more frequently, but raise the enthalpy  $H$  of the grain only by a small amount. X-ray absorption, on the other hand, is a relatively rare event, but accompanied by a big jump in  $H$ . Temperature distributions  $P(T)$  are shown in Fig. 17 for a flux  $F = 10^4 \text{ erg cm}^{-2} \text{ s}^{-1}$  corresponding to a luminosity  $L = 2.4 \times 10^{11} L_{\odot}$  at a distance of 100pc. The photon energies vary between 10 and 80eV. Grains much above the evaporation temperature of the solid ( $\sim 2000 \text{ K}$ ) are, of course, unrealistic.

The distributions  $P(T)$  in Fig. 17 display a kink at the temperature where the thermal energy of the grain equals  $h\nu$ . Still higher grain (momentary) temperatures are achieved when a second photon is absorbed before the grain has cooled off from the excitation by the first.

Fig. 18 displays the integral  $I_{\text{ev}}$  in equation (2) as a function of photon energy  $h\nu$  for various fluxes and two grain sizes. The important point is here that for the smallest graphite grains with  $5\text{\AA}$  radius (65 carbon atoms),  $I_{\text{ev}}$  grows very rapidly in the range from 20 to 40eV and then declines only gradually. The energy of photons,  $\langle h\nu \rangle$ , emitted by the hottest O stars ( $T_{\text{eff}} = 5 \times 10^4 \text{ K}$ ) is only 16 eV when averaged over the total spectrum, and equals 22 eV when averaged over the Lyman continuum ( $\lambda < 912\text{\AA}$ ). These numbers are thus upper limits for the radiation field in a starburst. Furthermore, the stellar flux of an O star plummets at wavelengths below  $228\text{\AA}$ , or above  $h\nu = 54.1 \text{ eV}$ , when helium becomes doubly ionized. AGNs, on the other hand, have a spectrum typically declining with  $\nu^{-0.7}$  and emit copious amounts of extreme UV and soft X-ray photons as witnessed by the observation of fine structure lines from ions with high ( $> 100 \text{ eV}$ ) ionization potentials.

We conclude from Fig. 18 that small graphite grains ( $5\text{\AA}$  radius) survive in a starburst as long as fluxes are below  $\sim 10^4 \text{ erg cm}^{-2}$ , but they will be destroyed near an AGN of the same flux  $F$ . The fate of PAHs of equivalent mass is similar (see Fig. 19). Bigger grains (see curves for

**Fig. 20.** Optically thin dust emission (full line) between 5 and  $15\ \mu\text{m}$  in a starburst (top) and an AGN (bottom) at various distances to the central heating source. The total luminosity is  $L = 10^{11}L_{\odot}$ . The emission of large grains, representing the continuum, is shown dashed.

$10\ \text{\AA}$  radius in Fig. 18) are much more resistive. They need higher fluxes to get vaporized and survive in a starburst environment.

## 7. Radiative transfer models

Here we present comprehensive model calculations for the mid-infrared emission of starburst and AGN radiation environments in the optical thin and optical thick regime.

### 7.1. Optically thin dust emission

In a first attempt to understand and to illustrate the influence of the hardness of the radiation field, we compute the optically thin dust emission at various distances from the source. A point-like heating source of total luminosity  $L = 10^{11}L_{\odot}$  has either the spectrum of an OB star ( $T_{*} = 25\,000\ \text{K}$ ) to mimic a starburst, or of an AGN with  $L_{\nu} \propto \nu^{-0.7}$  in the range from  $10\ \text{\AA}$  to  $\sim 2\ \mu\text{m}$  (the exact upper limit is unimportant as the dust has little extinction there). The distance to the source, and thus the flux which the dust receives, is varied from 4 to 100 pc.

For simplicity we consider in this section only two dust components: Large carbon grains with a  $n(a) \propto a^{-3.5}$  size distribution and radii between 300 and  $2400\ \text{\AA}$ , and PAHs consisting of 100 C and 28 H atoms and an abundance of 10% of the large carbon grains. The spectra are shown in Fig. 20. They are in arbitrary units and normalised at the maximum.

One notices that large grains become hotter as the radiation field hardens. At a distance of 4 pc to the heating source, PAHs invariably evaporate, at 10 pc evaporation occurs only near an AGN, and at 100 pc they survive in both environments, starburst and AGN.

### 7.2. Optically thick dust emission

Nuclei of luminous infrared galaxies are generally dust enshrouded and not transparent. Radiative transfer calculations of optically thick dusty nuclei have been carried out in various approximations (Krügel & Tutokov 1978, Rowan-Robinson & Crawford 1989, Pier & Krolik 1993, Loar & Draine 1993, Granato & Danese 1994, Krügel & Siebenmorgen 1984, Siebenmorgen et al. 1997, Silva et al. 1998, Efstathiou et al. 2000, Ruiz et al. 2001, Siebenmorgen et al. 2001, Nenkova et al. 2002).

In the subsequent spherical models, for starbursts and AGNs, the total luminosity is again  $10^{11}L_{\odot}$ . The dust cloud has a constant density, a visual extinction of  $A_V \sim 25\ \text{mag}$  (from the surface to the centre), and an outer cloud

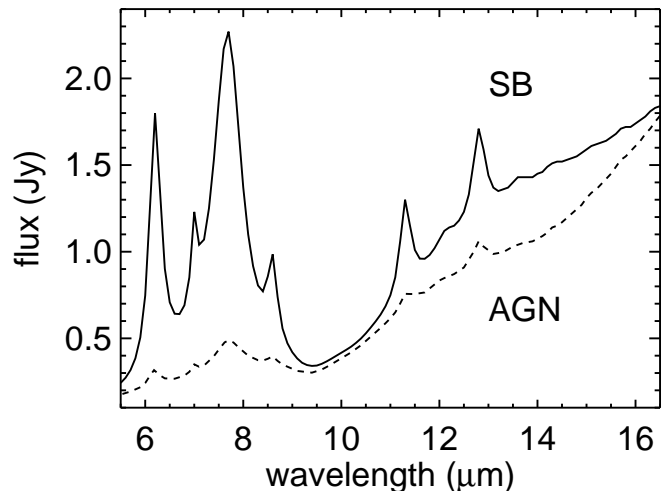


**Fig. 21.** Comparison of radiative transfer model spectra of dusty starbursts (solid) and AGN (dashed). In both models the visual extinction towards the cloud centre is  $A_V = 25\ \text{mag}$  and the luminosity is  $L = 10^{11}L_{\odot}$ . Spectra are calculated for a distance of 50 Mpc.

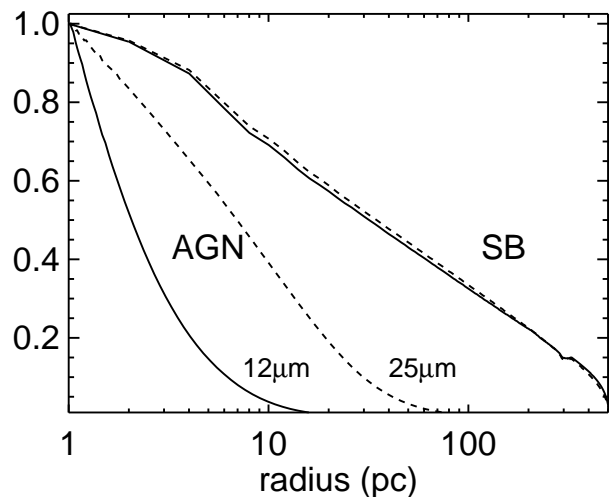


**Fig. 22.** Normalised intensities at 12 (solid lines) and  $25\ \mu\text{m}$  (dashed lines) for starbursts and AGN models as presented in Fig. 21. At both wavelengths the predicted FWHM of the starburst galaxy is much larger than for the AGN.

radius of 500 pc. To be a bit more realistic the dust consists here, besides large carbon grains, also of large silicate grains of the same size distribution and with a 12% larger total volume. Absorption and scattering efficiencies are calculated using Mie theory and optical constants by Loar & Draine (1993). In addition, there are small graphites and small silicates of  $10\ \text{\AA}$  radius, with an abundance of

0.5% that of the large carbon grains. PAH parameters are as described in the previous section.

The radiative transfer in a dust cloud around a starburst is computed following Siebenmorgen et al. (2001), around an AGN after Siebenmorgen et al. (1997) and the inclusion of soft X-rays as in this work. The major difference between both radiative transfer models is that AGN are heated by a central source whereas starburst galaxies are heated by stars which are distributed over a large volume. In case of a starburst, each of the OB stars have a uniform luminosity of  $20\,000 L_{\odot}$  and a stellar temperature  $T_* = 25\,000\text{ K}$ . The stellar density changes with galactic radius  $r$  up to  $500\text{ pc}$  from the center like  $\propto 1/r$  (there must be a cutoff at  $r = 0$ , but its exact position is unimportant). Each OB star is surrounded by a *hot spot* of constant dust density, corresponding to  $n(\text{H}) \sim 10^4\text{ cm}^{-3}$ . The size of the hot spot is determined by the condition of equal heating of the dust from the star and from the radiation field in the galactic nucleus. As for the AGN models, the inner radius of the hot spots is given by the photo-destruction or evaporation radius of the grains.

Our model spectrum for the starburst and the AGN is displayed in Fig. 21. The starburst shows strong PAH emission and a continuum which rises steeply beyond  $10\mu\text{m}$ , whereas the AGN is almost free of PAH emission. Cross cuts over the model nuclei, at various wavelengths, are shown in Fig. 22. At  $12\mu\text{m}$  and  $25\mu\text{m}$ , the AGN is much more compact than the starburst. Therefore the mid-infrared size may be used to distinguish between the two kinds of energy sources. This statement holds unless the stars are distributed by more than a few pc.

## 8. Conclusion

We presented mid infrared imaging and spectroscopy for a sample of 23 galactic nuclei. The observations were obtained with the ISO ( $14'' - 24''$  resolution) and with TIMMI2 at the 3.6m ESO telescope ( $3''$  and  $0.5''$  resolution for spectroscopy and imaging, respectively). The galaxies are mostly starbursts and AGNs, with apparent mid-infrared fluxes of  $20\text{ mJy}$  or more. Our main results are:

*a)* Seyfert nuclei are dominated by a compact core while starbursts do not display such a central concentration; they are usually spatially resolved by TIMMI2.

*b)* Almost all our ISO spectra (18 out of 19) are marked by bands at  $6.2$ ,  $7.7$ ,  $8.6$  and  $11.3\mu\text{m}$ , generally attributed to PAHs. In the TIMMI2 spectra, which refer to the innermost nuclear regions, these bands are present in starbursts, but not detected or significantly reduced in AGNs. This corroborates previous suggestions that PAHs evaporate much easier in the hard photon environment of an AGN, but are often able to survive in a starburst.

*c)* Applying a simple criterion for dust evaporation, we quantify the conditions under which small grains are photo-deconstructed in a monoenergetic hard radiation field. Analyzing their temperature distributions, we find that PAHs or very small graphite particles with less than 100

carbon atoms cannot survive if the photons have energies above  $20\text{ eV}$  and their flux is greater than  $10^3\text{ erg cm}^{-2}\text{ s}^{-1}$ . The detection or non-detection of PAH bands can thus serve as a diagnosis whether a galaxy is predominantly powered by an AGN or a starburst. Of course a very dense stellar cluster provides a high radiative density and destroys PAH (Siebenmorgen 1993). Therefore the dividing line between AGN and starbursts is not sharp, as demonstrated by the nuclear spectrum of M83 and Circinus.

*d)* In radiative transfer models that include soft X-rays and incorporate the above dust evaporation criterion, the starburst galaxies show PAH bands everywhere, and in the mid-infrared they are stronger and more extended than AGNs of the same luminosity.

*e)* The [S IV] and [Ne II] fine structure lines at  $10.5$  and  $12.8\mu\text{m}$ , which can still be excited in an O star environment, are in both types of galaxies generally stronger in the large (ISO) aperture spectra indicating that their emission comes from outside the nucleus.

*Acknowledgements.* PIA is a joint development by the ESA Astrophysics Division and the ISOPHT Consortium. This research has made use of the NASA/IPAC Extragalactic Database (NED) which is operated by the Jet Propulsion Laboratory, California Institute of Technology, under contract with the National Aeronautics and Space Administration.

## References

- Antonucci R.R.J., Miller J.S., 1985, ApJ 297, 621  
 Alloin D., Pantin E., Lagage P.O., Granato G.L., 2000, A&A 363  
 Bock J.J., Neugebauer G., Matthews K., et al., 2000, ApJ 120, 2919  
 Cesarsky C., Abergel A., Agnese P., et al., 1996, A&A 315, L32  
 Cohen M., Walker R.G., Carter B., Hammersley P., Kidger M., Noguchi L., 1999, AJ 117, 1864  
 Condon J.J., Helou G., Sanders D.B., Soifer B.T., 1996, ApJS 103, 81  
 Contini M., Contini T., 2003, MNRAS 342, 299  
 Clavel J., Schulz B., Alteri B., et al., 2000, A&A 357, 839  
 Genzel R., Cesarsky C., 2000, ARA&A 38, 761  
 de Graauw T., Haser L.N., Beintema D.A., et al., 1996, A&A 315, L49  
 Dwek E., Smith R.K., 1996, ApJ 459, 686  
 Efsthathiou A., Rowan-Robinson M., Siebenmorgen R., 2000, MNRAS 313, 734  
 Elbaz D., Cesarsky C. J., Chanical, P., et al., 2002, A&A 384, 848  
 Ferruit P., Wilson A.S., Mulchaey J., 2000, ApJS 128, 139  
 Granato G.L., Danese L., 1994, MNRAS 268, 235  
 Hasinger G., Burg R., Giacconi R., et al., 1998, A&A 329, 482  
 Heisler C.A., Vader J.P., 1995, AJ 110, 87  
 Heras A.M., Shipman R.F., Price S.D., et al., 1998, in: The Universe as seen by ISO, P.Cox & M.F.Kessler (Eds.), Paris, ESA-SP 427  
 Ho L.C., Ulvestad J.S., 2001, ApJS 133, 77  
 Horne K., 1986, PASP 98, 609  
 Hough J.H., Brindle C., Axon D.J., Bailey J., Sparks W. B., 1987, MNRAS 224, 1013

- Iwasawa K., Wilson A.S., Fabian, A.C., Young A.J., 2003, astro-ph/0306139
- Käuffl H.-U., Sterzik M., Siebenmorgen R., 2003, SPIE 4841, 117
- Kinney A.L., Bohlin R.C., Calzetti D., Panagia N., Wyse R.F.G., 1993, ApJS 86, 5
- Komossa S., Burwitz V., Hasinger G., et al., 2003, ApJ 582, L15
- Krügel E., Tutokov A.V., 1978, A&A 63, 375
- Krügel E., Siebenmorgen R., 1994, A&A 282, 407
- Kukula M.J., Pedlar A., Baum S.A., O’Dea C.P., 1995 MNRAS 276, 126
- Laurent O., Mirabel F.A., Charmandaris V., et al., 2000, A&A 359, 887
- Laureijs R.J., Watson D., Metcalfe L., McBreen B., O’Halloran B., 2000, AA 359, 900
- Lemke D., Klaas U., Abolins J., et al., 1996, A&A 315, L64
- Levenson N.A., Weaver K.A., Heckman T.M., 2001, ApJS 133, 269
- Loar A., Draine B.T., 1993, ApJ 402, 441
- Lutz D., 1999, in: The Universe as seen by ISO, P.Cox & M.F.Kessler (Eds.), Paris, ESA-SP 427, 623
- Lutz D., Sturm E., Genzel R., et al., 2000, ApJ 536, 697
- Markarian B.E., Lipovetskii V.A., Stepanian J.A., et al., 1989, Soobsch. Spets. Astrof. Obs. 62, 5
- Matt G., Fabian A.C., Guainazzi M., et al., 2000, MNRAS 318, 173
- Miles J.W., Houck J.R., Hayward T.L., Ashby M.L.N., 1996, ApJ 465, 191
- Moorwood A.F.M., Oliva E., 1994, Infrared Phys. Tech., 35, 349
- Moorwood A.F.M., Lutz D., Oliva E., et al., 1996, A&A 315, L125
- Moran E.C., Barth A.J., Kay L.E., Filippenko A.V., 2000 ApJ 391, L73
- Mulchaey J.S., Wilson A.S., Tsvetanov Z., 1996, ApJS 102, 309
- Nenkova M., Ivezić Z., Elitzur M., 2002, ApJ 355, 456
- Oliva E., Origlia L., 1998, A&A 332, 460
- Oliva E., Origlia L., Maiolino R., Moorwood A.F.M., 1999, A&A 350, 90
- Pfefferkorn F., Boller T., Rafanelli P., 2001, A&A 368, 797
- Pier E.A., Krolik J.H., 1993, ApJ 418, 673
- Regan M.W., Mulchaey J.S., 1999, AJ 117, 2676
- Reimann H.-G., Linz H., Wagner R., et al., 2000, SPIE 4008, 1132
- Rigopoulou D., Spoon H.W.W., Genzel R., et al., 1999, AJ 118, 2625
- Roche P.F., Aitken D.K., Smith C.H., Ward M.J., 1991, MNRAS 248, 606
- Rowan-Robinson M., Crwaford J., 1989, MNRAS 238, 523
- Ruiz M., Efstathiou A., Alexander D.M., et al., 2001, MNRAS 316, 49
- Sanders D.B., Mirabel I.F., 1996, ARA&A 34, 749
- Schinnerer E., Eckart A., Quirrenbach A., et al., 1997, ApJ 488, 174
- Schmitt H.R., Storchi-Bergmann T., Baldwin J.A., 1994, ApJ 423, 237
- Schutte W.A., Tielens A.G.G.M., Allamandola L.J., 1993, ApJ 415, 397
- Scoville N.Z., Evans A.S., Thompson R., et al., 2000, AJ 119, 991
- Siebenmorgen R., 1993, ApJ 408, 218
- Siebenmorgen R., Moorwood A., Freudling W., Käuffl H.U., 1997, A&A 325, 450.
- Siebenmorgen R., Krügel E., Zota V., 1999, A&A 351, 140
- Siebenmorgen R., Krügel E., Laureijs R., 2001, A&A 377, 735
- Silva L., Granato G.L., Bressan A., 1998, ApJ 506, 600
- Smith C.H., Aitken D.K., Roche P., 1989, MNRAS 241, 425
- Soifer B.T., Sanders D.B., Madore B.F., et al., 1987, ApJ 320, 238
- Soifer B.T., Neugebauer G., Matthews K., et al., 2000, ApJ 119, 509
- Soifer B.T., Neugebauer G., Matthews K., et al., 2002, AJ 124, 2980
- Spoon H.W.W., Keane, J. V. Tielens, A. G. G. M., et al., 2002, A&A 385, 1022
- Starck J., Siebenmorgen, R., Gredel R., 1997, ApJ 482, 1011
- Starck J.-L., Murtagh F., 2002, Astronomical Data and Image Analysis, Springer (ISBN 3-540-42885-2).
- Stacey, G.J., Swain M.R., Bradford C.M., et al., 1998, in: The Universe as seen by ISO, P.Cox & M.F.Kessler (Eds.), Paris, ESA-SP 427, 973
- Storchi-Bergmann T., Raimann D., Bica E.L.D., Fraquelli H.A., 2000, ApJ 544, 747
- Sturm E., Lutz D., Verma A., et al., 2002, A&A 393, 821
- Tacconi L.J., Genzel R., Tecza M., 1999, ApJ 524, 732
- Tecza M., Genzel R., Tacconi L.J., et al., 2000, ApJ 537, 178
- Thornley M.D., Förster-Schreiber N.M., Lutz D., et al., 2000, ApJ 539, 641
- Vader J.Frogel J.A., Terndrup D.M., Heisler C.A., 1993, AJ 106, 1743
- Verma A., Lutz D., Sturm E., et al., 2003, A&A 403, 829
- Voit G.M., 1991, ApJ 379, 122
- Winge C., Storchi-ergmann T., Ward M., Wilson A.S., 2000, MNRAS 316, 100

This figure "h4623\_f2.png" is available in "png" format from:

<http://arxiv.org/ps/astro-ph/0310546v1>



This figure "h4623\_f3.png" is available in "png" format from:

<http://arxiv.org/ps/astro-ph/0310546v1>

This figure "h4623\_f4.png" is available in "png" format from:

<http://arxiv.org/ps/astro-ph/0310546v1>

This figure "h4623\_f5.png" is available in "png" format from:

<http://arxiv.org/ps/astro-ph/0310546v1>

This figure "h4623\_f6.png" is available in "png" format from:

<http://arxiv.org/ps/astro-ph/0310546v1>

This figure "h4623\_f7.png" is available in "png" format from:

<http://arxiv.org/ps/astro-ph/0310546v1>

This figure "h4623\_f8.png" is available in "png" format from:

<http://arxiv.org/ps/astro-ph/0310546v1>

This figure "h4623\_f9.png" is available in "png" format from:

<http://arxiv.org/ps/astro-ph/0310546v1>

This figure "h4623\_f10.png" is available in "png" format from:

<http://arxiv.org/ps/astro-ph/0310546v1>



This figure "h4623\_f11.png" is available in "png" format from:

<http://arxiv.org/ps/astro-ph/0310546v1>

This figure "h4623\_f12.png" is available in "png" format from:

<http://arxiv.org/ps/astro-ph/0310546v1>

This figure "h4623\_f13.png" is available in "png" format from:

<http://arxiv.org/ps/astro-ph/0310546v1>

This figure "h4623\_f14.png" is available in "png" format from:

<http://arxiv.org/ps/astro-ph/0310546v1>

This figure "h4623\_f15.png" is available in "png" format from:

<http://arxiv.org/ps/astro-ph/0310546v1>

This figure "h4623\_f16.png" is available in "png" format from:

<http://arxiv.org/ps/astro-ph/0310546v1>

This figure "h4623\_f17.png" is available in "png" format from:

<http://arxiv.org/ps/astro-ph/0310546v1>

This figure "h4623\_f18.png" is available in "png" format from:

<http://arxiv.org/ps/astro-ph/0310546v1>



This figure "h4623\_f19.png" is available in "png" format from:

<http://arxiv.org/ps/astro-ph/0310546v1>

This figure "h4623\_f20.png" is available in "png" format from:

<http://arxiv.org/ps/astro-ph/0310546v1>